Journal of Alloys and Metallurgical Systems 1 (2023) 100005

Contents lists available at ScienceDirect

Journal of Alloys and Metallurgical Systems

journal homepage: www.journals.elsevier.com/journal-of-alloys-and-metallurgical-systems

The roles of solidification cooling rate and (Mn,Cr) alloying elements in the modification of β-AlFeSi and hardness evolvements in near-eutectic Al-Si alloys

R. Kakitani[a,*], A.V. Rodrigues[a,b], C. Silva[a], A. Garcia[a], N. Cheung[a]

[a] Department of Manufacturing and Materials Engineering, University of Campinas - UNICAMP, 13083-860 Campinas, SP, Brazil
[b] Federal Institute of Education, Science and Technology of São Paulo, IFSP, Bragança Paulista 12903-000, Brazil

ARTICLE INFO

Keywords:
Al-Si alloy
Fe/Mn/Cr alloying elements
Solidification
Microstructure
Hardness

ABSTRACT

High recycling rates worldwide underline the economic and environmental value of aluminum scrap. However, several alloying elements in recycled Al negatively affect the final properties of castings, among which Fe has the most permissive effect on the mechanical properties. The extremely restricted solid solubility of Fe in Al leads to the formation of brittle Fe-containing intermetallic compounds (IMCs), and a possible strategy is to use modifiers of harmful IMCs by alloying. The present work aims to investigate the substitutional characteristic of Fe, Mn, Cr in the α-IMC taking the Al-12 %Si alloy as a reference, i.e., by analyzing the directional solidification (DS) of binary (Al-12 %Si), ternary (Al-12 %Si-1 %Fe) and quaternary (Al-12 %Si-1 %Fe-1 %Mn and Al-12 %Si-1 %Fe-0.6 %Cr) alloys. For all DS alloys castings, the macrostructure is shown to be characterized by columnar grains associated with solidification cooling rates ($\dot{T}$) from 0.4 to 42.3 °C/s. The microstructure of the four alloys examined is shown to be typified by an α-Al dendritic matrix with interdendritic regions formed by α-Al, Si and different IMCs, which have been characterized and associated with the local $\dot{T}$. The evolvement of iron-containing IMCs morphologies according to the addition of alloying elements in Al-Si alloys, is as follows: plate-like for Fe, plate-like and Chinese script for Mn, and fishbone and trefoil/blocky for Cr. Experimental power laws equations are determined relating the primary (λ_1), secondary (λ_2) and tertiary dendritic arm spacings (λ_3) to $\dot{T}$, for any experimentally examined DS alloy casting. The microhardness (HV) of the alloys is correlated with λ_3 and Hall-Petch type equations are derived relating HV to both λ_3 and $\dot{T}$. The Al-12 %Si-1 %Fe-0.6 %Cr alloy achieved the highest HV among all the alloys examined.

1. Introduction

The global recycling of aluminum scrap has been increasing year by year due to several factors, such as: i) finite availability of bauxite, the main primary raw material used to make aluminum; ii) energy savings since remelting recycled aluminum saves almost 95 % of the energy required for the elaborative reduction of Al_2O_3; iii) the avoidance of red mud generation, a non-ecologically friendly residue from the electrolysis process; iv) the reduction in greenhouse gas emissions associated with the electricity consumption and subproducts from electrolysis; v) recycling aluminum-based automotive components from old and dismantled vehicles can reduce waste disposal in landfills [1–4]. However, several alloying elements in recycled aluminum negatively affect the final properties of the castings and some solutions have been proposed to address this issue. The conventional solution is to accept the impurities by adding primary aluminum for lowering their concentration [5]. On the other hand, this methodology is ineffective as it does not mitigate the inevitable accumulation of undesired elements in scrap metals recycling [6]. Therefore, removing unwanted elements seems to be the only path, but in some cases, this is not economically feasible, as for example iron [7].

Iron has the most permissive effect on the mechanical properties of Al-Si based alloys, which is a concern in the automotive industry due to the extensive applications of such alloys, such as in pistons. The extremely restricted solid solubility of iron in Al (about 10 ppm) leads to the formation of brittle Fe-containing intermetallic compounds (IMCs) such as the β-Al_5FeSi IMC, which consists of three-dimensionally interlinked thin platelets [8,9]. Considering the Al-Si-Fe ternary alloy

* Corresponding author.
E-mail address: rkakitani@fem.unicamp.br (R. Kakitani).

https://doi.org/10.1016/j.jalmes.2023.100005
Received 24 February 2023; Received in revised form 4 April 2023; Accepted 17 April 2023
Available online 18 April 2023

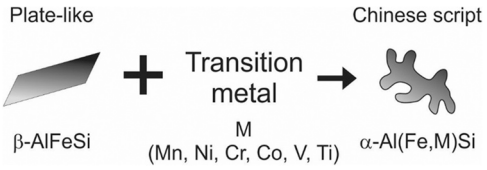

Fig. 1. Transformation of the plate-like β-AlFeSi into Chinese script α-Al(Fe,M)Si by modifying a transition metal (M).

system, Belov and coauthors reported in their book, that the solubility of iron, although still low in aluminum, varies considerably with temperature [9]. This solubility is different depending on the IMCs formed (Al_3Fe, α-AlFeSi and β-AlFeSi) but in general varies from 0.002 % to about 0.05 % in the temperature range of 400 °C to about 630 °C, respectively. This β-phase is detrimental to mechanical properties when formed in the primary stage due to its large size, but it has negligible influence as part of the eutectic mixture due to its small size [10]. Transition metals such as Mn, Ni, Cr, Co, V, and Ti have been added to Fe-contaminated Al-Si alloys to change the morphology of the β-particles. In other words, the strategy is to use modifiers of harmful IMCs by alloying [11]. For example, a less damaging morphology of Chinese script (Fig. 1) takes place when forming α-$Al_{15}(Fe,Mn,Cr)_3Si_2$, in which (Fe,Mn,Cr) denotes that Fe, Mn and Cr can replace each other in the same BCC crystal structure [12]. However, star-like and polyhedral morphologies are possible to be formed depending on the ratio between the alloying element: Fe and on the solidification cooling rate [13–15].

Due to the aforementioned substitutional characteristic of Fe, Mn, Cr in the α-IMC, the present work comparatively analyzes the following alloys: Al-12 %Si, Al-12 %Si-1 %Fe, Al-12 %Si-1 %Fe-1 %Mn and Al-12 %Si-1 %Fe-0.6 %Cr. It can be noted that the progressive addition of alloying elements consisting of binary (Al-12 %Si), ternary (Al-12 %Si-1 %Fe) and quaternary (Al-12 %Si-1 %Fe-1 %Mn and Al-12 %Si-1 %Fe-0.6 %Cr) alloys will permit a better understanding on the role played by each added element. This procedure has been previously implemented in our research group, such as in the Al-Si-Fe-V alloy system [16], a work that also focused on the recycling of Fe contaminated Al-Si alloys. The relatively high 1 % Fe content was chosen to simulate its accumulative effect in the scrap cycle. Regarding the Mn content, it is reported that it should not be less than half of that of iron [17] and for the Cr content, a Cr:Fe ratio not lower than 0.3 [10], i.e., a smaller amount of Cr than Mn is more effective in transforming β-AlFeSi into α-AlFeSi [18]. Working with Cr:Fe lower than 0.3, and associated with high cooling rates due to the high pressure die casting process, Timelli et al. [19] observed the formation of primary sludge particles and primary Alx(Fe,Mn,Cr)ySiz IMCs in Al-9 %Si-3 %Cu-Fe alloys. Generally, the increase in Mn, associated with the decrease in the solidification cooling rate, induces the formation of coarser Fe-IMCs [20]. Liu et al. [21] observed that the increase in cooling rate during the solidification of commercial 206 Al-Cu alloys with 0.15 % Fe decreases the formation of the β-AlFeSi IMC, but increases the α-AlFeSi IMC, for the seven Si:Mn ratios analyzed and six cooling rates ranging from 0.2 up to 7.5 °C/s. In Al-9 %Si alloys with 0.3 %Fe, even for a Mn:Fe ratio of 2:1 and high cooling rates, iron-rich needles were not totally depleted [22]. Analyzing an Al-7 %Si-1.2 %Fe alloy with Mn additions, Song and coauthors [23] realized that the β-AlFeSi IMC can be eliminated with the addition of 1.06 %Mn, but with reduction in ductility due the formation of a star-like Fe-IMC. However, a deeper analysis is needed when the solidification cooling rate is involved, since it may change the α-IMC morphology to polyhedral or star-like [15].

Thus, the present work not only takes into account the additions of Cr and Mn, but also focuses on the influence of a wide range of solidification cooling rates obtained through directional solidification under unsteady-state heat flow regime. Microstructural characterization of the IMCs has been provided by X-Ray Diffraction, Optical and Scanning Electron Microscopies and Energy Dispersive Spectroscopy. The hardness behavior is discussed considering not only the nature and modification of the IMCs but also the evolution of the dendritic growth. To the best of the present authors´ knowledge, such an extensive and comparative analysis determining correlations involving solidification thermal parameters, microstructural growth and hardness response has not been yet performed considering the additive alloying effect of different elements in Al-Si based alloys.

2. Materials and methods

The nominal compositions of the alloys studied in this work are Al-12 wt%Si, Al-12 wt%Si-1 wt%Fe, Al-12 wt%Si-1 wt%Fe-1 wt%Mn and Al-12 wt%Si-1 wt%Fe-0.6 wt%Cr. The compositions of each commercially pure metal used to prepare these alloys are shown in Table 1. Firstly, to produce each alloy, 800 g of aluminum was placed inside an alumina coated SiC crucible and taken to an electric resistance furnace at 800 °C to be melted. After this, according to the composition of each alloy, pieces of Si, Fe, Mn and Cr were added to the molten aluminum. To ensure homogenization, the addition of each element occurred individually, followed by stirring the resulting liquid bath using an alumina-coated stainless-steel bar and its return into the furnace for about 45 min. Argon gas was injected into the molten mixture for approximately 2 min to eliminate possible trapped gases. Each molten alloy was poured into a stainless-steel cylindrical split mold with dimensions of 60 mm internal diameter, 150 mm height and 3 mm wall thickness, whose internal surface was previously coated with alumina to minimize the radial heat losses during solidification. The main components of the water-cooled upward directional solidification apparatus, including the properly positioned mold, are schematically represented in Fig. 2.

The temperature controller of the electric furnace heaters allows the melting of the alloys with the desired melt superheat. The solidification process starts when the electric heaters are switch off and the water flow, which is controlled by the water flow meter, starts at the bottom of the mold extracting the released heat. A water flow of 20 L/min is set when 10 % of superheat above the liquidus temperatures of each alloy is reached. During the cooling process, K-type thermocouples, previously placed at different positions (P) along the length of the mold, having the cooled surface of the casting as reference, are responsible for continuously monitoring the temperatures during solidification progress. The thermal profiles (temperature–time) are recorded through a data logging system, connected to a computer, at a frequency of 5 Hz. To obtain the solidification thermal parameters, the data acquired during the experiments are further processed allowing the determination of growth rates (v) and cooling rates ($\dot{T}$) over the length of each directionally solidified (DS) alloy casting. At the time when the liquidus temperature (T_L) is reached at each thermocouple location (P), $\dot{T}$ is determined by the derivative of the cooling curve with respect to time

Table 1
Chemical composition (in wt%) of the elements used to prepare the alloys.

Element	Al	Si	Fe	Mn	Cr	Cu	Zn	Ni	S	P
Al	Bal.	0.055	0.073	-	-	0.01	0.05	0.006	-	-
Si	0.084	Bal.	0.21	-	-	-	-	0.016	-	-
Fe	0.0003	-	Bal.	0.002	-	-	-	0.002	-	-
Mn	-	-	-	Bal.	-	-	-	-	0.033	0.0026
Cr	0.39	0.06	0.19	-	Bal.	0.002	0.004	-	0.01	0.002

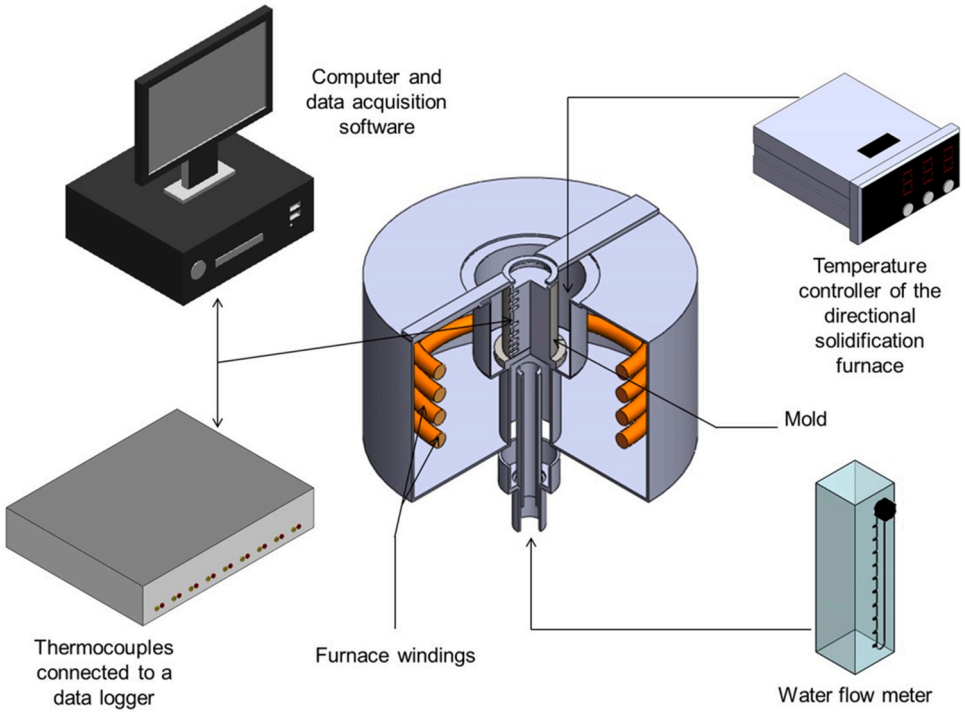

Fig. 2. Split stainless-steel mold and the main components of the water-cooled upward directional solidification apparatus.

(t). A profile of P × t is obtained considering the time for the liquidus temperature to pass through each thermocouple, and v, in turn, is a result of the time derivative of the P × t profile, i.e., represents the evolution in time of T_L from the bottom towards the top of the casting.

Longitudinal and transverse microstructures were analyzed on samples extracted at different positions from the metal/mold interface (water cooled surface) to the top of DS castings. Silicon carbide papers from 100 to 1200 mesh were used to grind the samples and diamond paste (1 and 3 μm) was employed for polishing. As shown by the schematic representation of Fig. 3, a decreasing profile of cooling rates (from the cooled surface of the casting) is accompanied by an increasing profile of the length scale of a dendritic microstructure, that is, higher cooling rates promote more refined microstructures while lower cooling rates, coarser microstructures. The composition of the alloys was verified in a Shimadzu μ-EDX 1300 X-ray fluorescence equipment. Optical images of longitudinal and transverse sections were obtained through an Olympus Inverted Metallurgical Microscope (model 41GX). Intermetallic compounds (IMCs) were characterized by a ZEISS-EVO-MA15 Scanning Electron Microscope (SEM) equipped with a QUANTA 650 FEG Energy Dispersive X-Ray Spectrometer (EDS), used to quantify, and

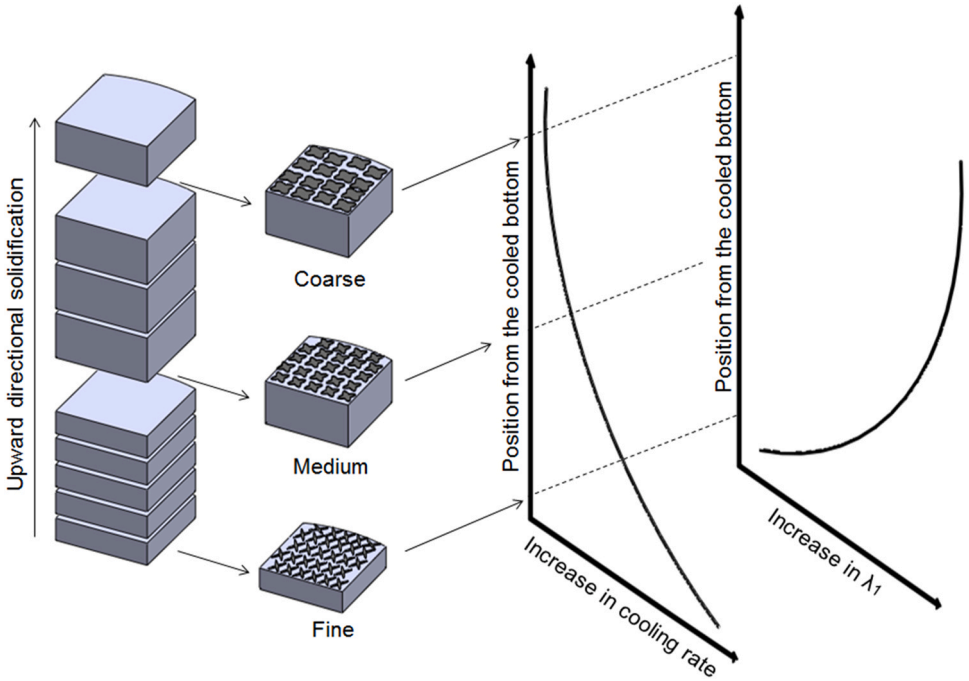

Fig. 3. Schematic representation of the samples and the relation between position from the metal/mold interface x cooling rates/microstructural length scale represented by λ_1.

determine the distribution of elements in the microstructures. Taking similar cooling rates as parameter, three positions (bottom, medium and top of castings) of each alloy were characterized by X-Ray Diffraction – XRD using a X'Pert-MDP diffractometer to acquire the patterns at the 2θ range from 20° to 90° with a Cu-Kα radiation with a wavelength of 0.15406 nm.

The triangle method was employed to obtain the primary dendritic arm spacings (λ_1) on transverse sections of the samples and the linear intercept method [24] was carried out to acquire the secondary (λ_2) and the tertiary (λ_3) dendritic arm spacings on the longitudinal and transverse sections, respectively. Considering at least, 8 different regions (over 600 measurements), the size of the different IMCs was measured based on the area and the circularity was calculated using Eq. (1).

$$\text{Circularity} = 4*\pi*\text{Area}/\text{Perimeter}^2 \quad (1)$$

Vickers microhardness tests were performed using a Shimadzu HMV-2 model hardness tester with a load of 0.5 kgf and a dwell time of 15 s. The average of at least 20 measurements was the hardness value adopted for each representative sample.

3. Results and discussion

3.1. Phases characterization

In the unsteady-state directional solidification experiments, it was possible to obtain $\dot{T}$ from 0.4 to 42.3 °C/s along the length of the castings. Although the different cooling rate profiles (Fig. 4a), there is a common range between 1.2 and 15.8 °C/s. In this range, $\dot{T}$ above 10 °C/s can be classified as a high cooling rate and $\dot{T}$ < 4 °C/s as a low cooling rate. Even for the lowest cooling rates, columnar grains prevailed along the length of the DS alloys castings, as can be seen in Fig. 4b–e. Table 2 shows the chemical composition of the alloys and segregation was not detected along the length of the DS castings.

Fig. 5 depicts the typical microstructure of the four alloys examined, characterized by an α-Al dendritic matrix with interdendritic regions formed by α-Al, Si and IMCs. For the Al-12 %Si alloy, a small fraction of IMC was observed to occur, due to the presence of Fe in both aluminum and silicon (Table 1), which probably promoted the formation of the β-AlFeSi IMC. The IMCs in the Al-12 %Si-1 %Fe alloy exhibited a plate-like morphology (detail of Fig. 5b) with two types of length: shorter than 50 μm, present in all the analyzed samples, and longer than 100 μm, mainly found in samples that solidified at $\dot{T}$ > 11 °C/s and outside the interdendritic region. In the Al-12 %Si-1 %Fe-1 %Mn alloy samples, besides the plate-like phase, an IMC with Chinese script morphology was observed to occur, as can be seen in the detail of Fig. 5c. The arrangement of the primary IMCs and consequently a possible evidence of growth direction seems to be affected during the process of ramification of the dendrites, which occurs after the formation of IMCs. At high $\dot{T}$, the plates are the major fraction, and as the cooling rate decreased, the fraction of Chinese script IMC progressively increased until it becomes the majority. At this point, it is obvious that 1 %Mn was not capable to completely change the plate-like IMCs. On the other hand, a more effective modification was observed in the microstructure of the Al-12 %Si-1 %Fe-0.6 %Cr alloy, with the absence of plates and predominance of compact IMCs (detail of Fig. 5d). Fig. 6 is a schematic showing the evolution of the IMCs with respect to $\dot{T}$, in the DS Al-12 %Si-1 %Fe-0.6 %Cr alloy casting. In order to complement the IMCs characterization, the results of the EDS analysis will be shown later in this section. At a first view, the compact morphology could be described as Chinese script but a deep etching (bottom of the second column in Fig. 6) revealed a connected structure, like a fishbone. The fishbone morphology has already been mentioned in other studies [25–27] and was usually associated with the improvement of mechanical properties. Normally, the fishbone morphology is more compact and rounded than the plate-like and blocky IMCs, which can reduce the local stress raiser. In our previous study [25], the partial transformation of plate-like Al_3Ni into fishbone Al_3Ni improved the ultimate tensile strength of the Al-11 %Si-5 %Ni alloy. In addition, Yang et al. [27] noticed that the addition of Cr into an Al-Si-Cu-Mg-Ni-Fe alloy promoted the formation of α-Al(Fe,Cr)Si fishbone instead of needle-like β-AlFeSi. Consequently, the elongation increased up to 53.5 %. A trefoil-type and blocky IMCs were also present in the microstructure of the DS Al-12 %Si-1 %Fe-0.6 %Cr alloy casting, but it proved to be quite sensitive to the cooling rate, appearing at 42.3 °C/s and below 5 °C/s, outside the interdendritic regions. Unlike the refined fishbone, the trefoil/blocky IMC was coarse and reached more than 50 μm^2 in size.

Another contribution of the alloying elements, mainly Fe, was the modification of the eutectic Si (Fig. 5), in which the length of the Si particles was reduced and the number of particles per area increased.

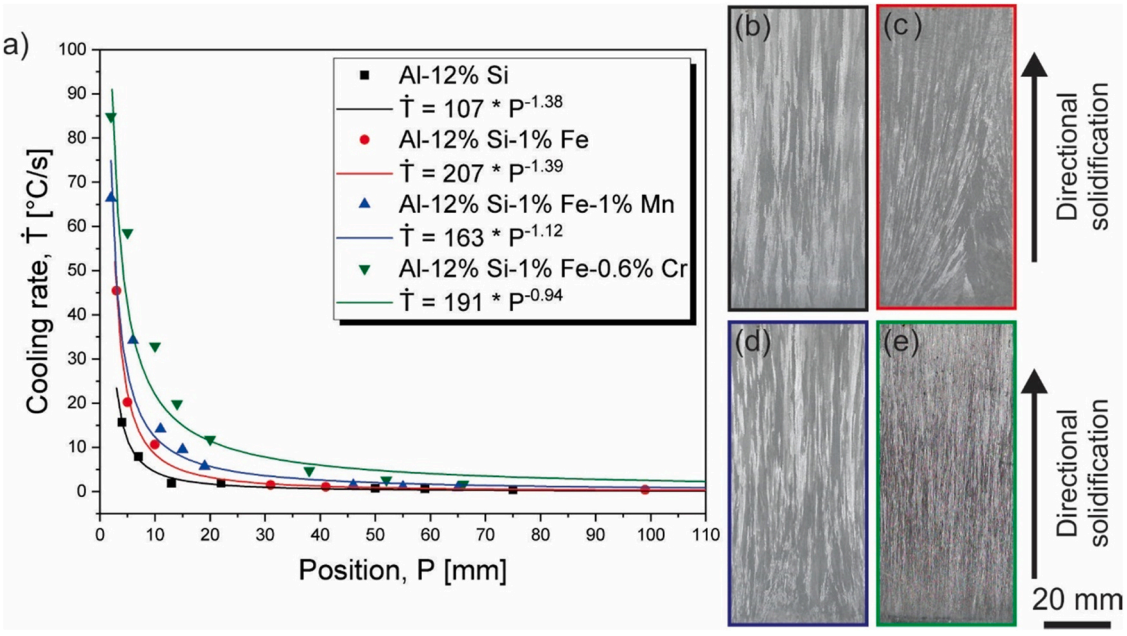

Fig. 4. a) Experimental cooling rate profiles of the alloys, and macrostructures of the DS castings of b) Al-12 %Si, c) Al-12 %Si-1 %Fe, d) Al-12 %Si-1 %Fe-1 %Mn and e) Al-12 %Si-1 %Fe-0.6 %Cr alloys.

Table 2
Chemical compositions of the alloys, in wt%.

Element	Al-12Si	Al-12Si-1Fe	Al-12Si-1Fe-1Mn	Al-12Si-1Fe-0.6Cr
Al	Balance			
Si	11.9 ± 0.3	12.0 ± 0.3	12.2 ± 0.5	12.1 ± 0.4
Fe	0.2 ± 0.1	1.2 ± 0.2	1.2 ± 0.3	1.1 ± 0.1
Mn	-	-	0.9 ± 0.2	-
Cr	-	-	-	0.64 ± 0.04

Zhang and collaborators [28] proposed that clusters of AlFeSi – the inception of β-AlFeSi – are precursors of the eutectic Si, supporting the nucleation and growth. So, it seems that the different IMCs of the alloys were able to modify the eutectic Si.

In Fig. 7, the simulation of the equilibrium phase fraction, by the JMatPro software, pointed out that the β-AlFeSi IMC precipitates in the three Fe-containing alloys, while the less deleterious α-Al(Fe,Mn)Si is solely formed in the Al-12 %Si-1 %Fe-1 %Mn alloy casting. By adding 0.6 %Cr to the Al-12 %Si-1 %Fe alloy, the $Al_{13}Cr_4Si_4$ IMC is the fourth phase to compose the final microstructure, without a phase transformation of the α-Al(Fe,Cr)Si IMC. To confirm the phases, Fig. 8 shows the XRD profiles of three samples of each alloy. Despite the different solidification cooling rates of each sample, no remarkable differences in the XRD profiles have been detected. The main peaks in Al-12 %Si alloy (Fig. 8a) matched with the α-Al and Si phases, and only two peaks were correlated with the β-AlFeSi IMC, in agreement with the low fraction found in the microstructure. As expected, due to the higher volume of plates, there were more peaks related to the β-AlFeSi IMC in the Al-12 %Si-1 %Fe alloy (Fig. 8b). Even though the XRD profiles confirmed the same phases in the simulation of the Al-12 %Si-1 %Fe-1 %Mn alloy, only three phases were identified in the DS Al-12 %Si-1 %Fe-0.6 %Cr alloy casting, i.e. α-Al, Si and α-Al(Fe,Cr)Si, as can be seen in Fig. 8c–d. The $Al_{13}Cr_4Si_4$ phase according to Fig. 7d, in equilibrium conditions, has the lowest solid fraction of all phases, which may have contributed to the lack of detection by the XRD equipment, due to its low sensibility for tiny phases quantities. Additionally, it is worth noting that the cooling conditions of the directional solidification provided unsteady-state heat flow conditions that altered the solidification kinetics, promoting or hindering the formation of phases.

The SEM-EDS results of the Fe-containing alloys are shown in Fig. 9. The main focus of the SEM-EDS analysis was the IMCs, but the solid solution of Si in α-Al was shown to be 0.9 ± 0.3 wt%. In the Al-12 %Si-1 %Fe alloy, the plate-like IMC had an atomic proportion of Fe/Si between 0.3 and 0.5, however, it is worth noting that the amount of Si could be overestimated due to the pear-shaped volume interaction of the X-Ray beam. The #1 point is located in a large β-AlFeSi plate (Fig. 9a) and Fe/Si is close to 0.5. Despite the difference in morphology, in the Al-12 %Si-1 %Fe-1 %Mn alloy, Mn was detected in both types of IMC. In the plates, the atomic proportion (Fe + Mn)/Si was 0.3–0.5, whilst in the Chinese script phases, the ratio was higher than 1.0 (#2 and #3, respectively, in Fig. 9b). The literature reports the α-AlFeSi phases as Al_8Fe_2Si or $Al_{12}Fe_3Si_2$ (hexagonal) and $Al_{15}Fe_3Si_2$ (body-centered cubic), where Mn can replace Fe and Fe:Si > 1 [29–31]. Therefore, based on the morphology and atomic composition, it is assumed that the plates are β-AlFeSi and the Chinese script phase is α-Al(Fe,Mn)Si. From the XRD profiles, the α-Al(Fe,Cr)Si phase is the only IMC in the Al-12 %Si-1 %Fe-0.6 %Cr alloy, despite having three different morphologies. In Fig. 9c, points #4 and #5, the SEM-EDS analysis revealed that (Fe + Cr):Si > 1 and the amounts of Si and Cr are higher in the trefoil/blocky phase than in the fishbone IMC. Since the trefoil/blocky precipitated at 42.3 °C/s and $\dot{T} < 5$ °C/s, in the highest cooling rate the solute rejection was very high and a few Cr rich nuclei may be promoted, thus developing the coarser α-Al(Fe,Cr)Si IMC. For $\dot{T} < 5$ °C/s, it seems that the kinetic conditions permitted the formation of Cr-rich nuclei through diffusion in the liquid. The high amount of Fe in the IMCs excludes the possibility of occurrence of the $Al_{13}Cr_4Si_4$ IMC.

In the foundry industry, large Fe-rich IMCs are known as sludge. The formation of sludges occurs above the alloy liquidus temperature and is influenced by Fe, Mn, and Cr concentrations [32,33]. Eq. (2) is the sludge factor (SF), an empirical equation that evaluates how much sludge could precipitate [34].

$$SF = 1 * (wt\%Fe) + 2 * (wt\%Mn) + 3 * (wt\%Cr) \quad (2)$$

The Al-12 %Si-1 %Fe-1 %Mn and Al-12 %Si-1 %Fe-0.6 %Cr alloys have similar SF values: 3 and 2.8, respectively – but the precipitation conditions and fraction of sludges (large plates and trefoil/blocky) are different. In the literature, there is no consensus if high cooling rates are favorable conditions to form sludges. At the range of 0.5–40 °C/s,

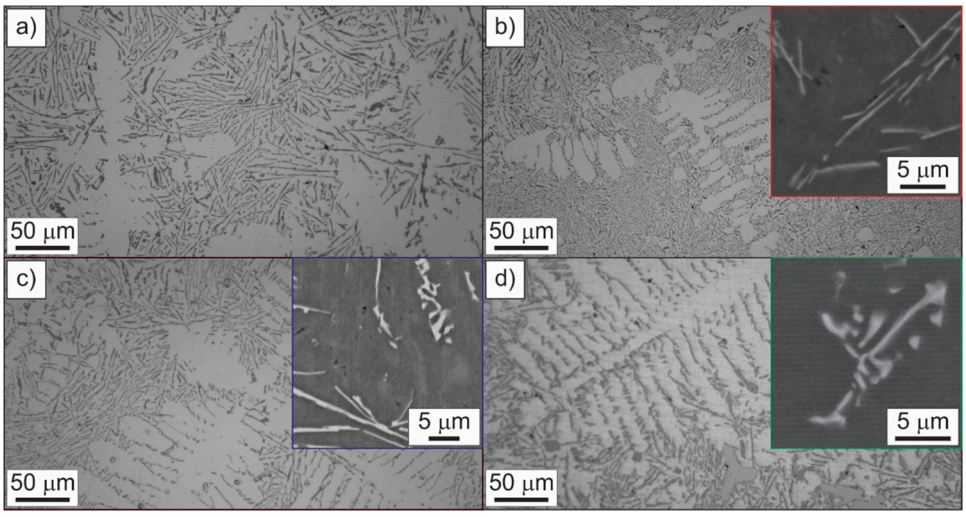

Fig. 5. Typical microstructures of: a) Al-12 %Si, b) Al-12 %Si-1 %Fe, c) Al-12 %Si-1 %Fe-1 %Mn and d) Al-12 %Si-1 %Fe-0.6 %Cr alloys, solidified at 3.5 °C/s. The details show the main intermetallics found in each DS alloy casting.

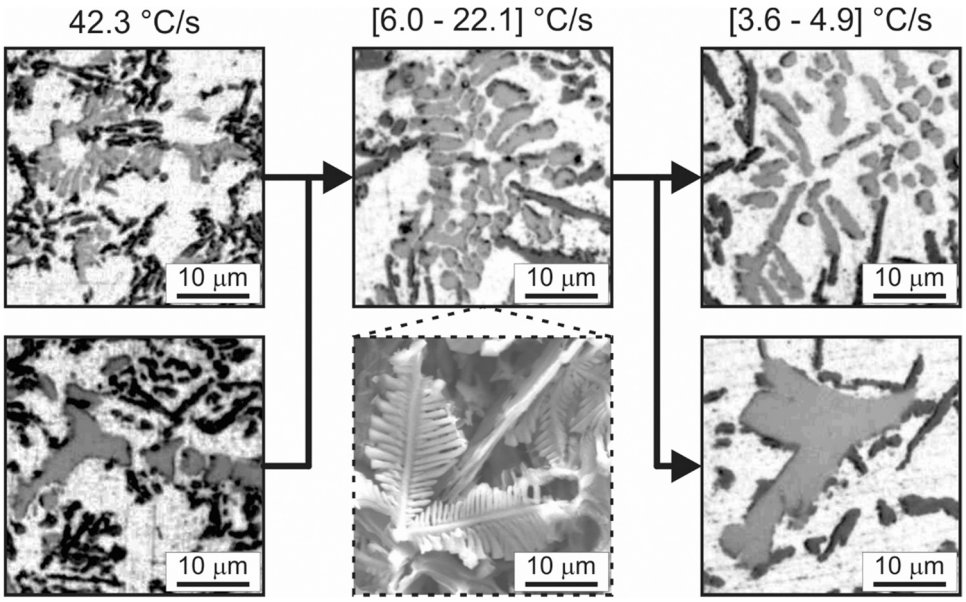

Fig. 6. Evolution of the IMCs in the DS Al-12 %Si-1 %Fe-0.6 %Cr alloy casting as a function of the cooling rate. The detail (bottom of the second column) exhibits the IMCs after deep etching.

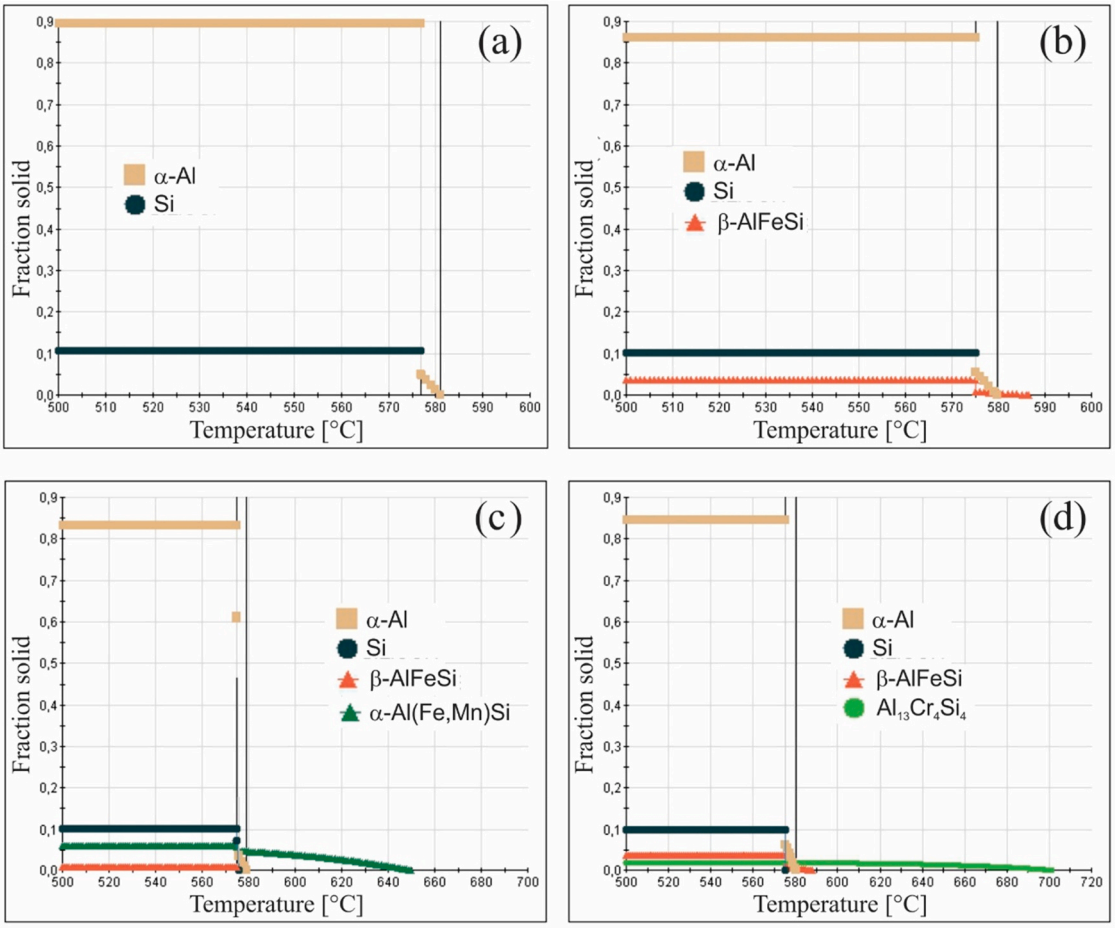

Fig. 7. Equilibrium phase fraction (calculated by the JMatPro v. 13.2 software) following the decrease in temperature for: a) Al-12 %Si, b) Al-12 %Si-1 %Fe, c) Al-12 %Si-1 %Fe-1 %Mn and d) Al-12 %Si-1 %Fe-0.6 %Cr alloys.

Ferraro et al. [33] observed that the fraction of sludges increases as the cooling rate increases. However, Timelli et al. [32] verified in differential scanning calorimetry tests (2, 10, 20 °C/min) an opposite behavior, i.e., formation of sludges only for the lowest $\dot{T}$. Based on the alloys of the present study, it seems that Cr has a stronger role on sludges formation. So, a better comprehension of the influence of the alloying elements is an essential task.

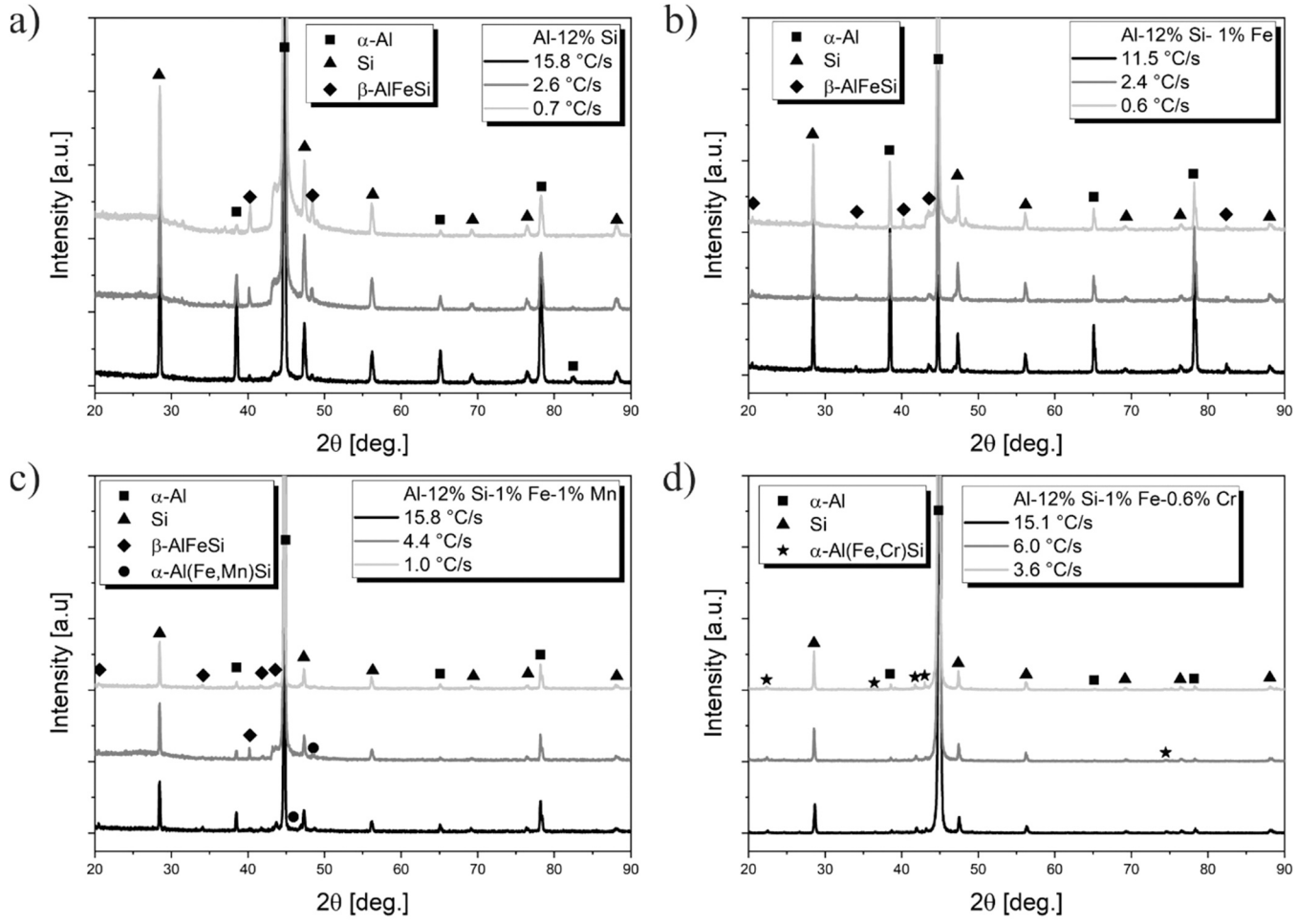

Fig. 8. XRD profiles for: a) Al-12 %Si, b) Al-12 %Si-1 %Fe, c) Al-12 %Si-1 %Fe-1 %Mn and d) Al-12 %Si-1 %Fe-0.6 %Cr alloys.

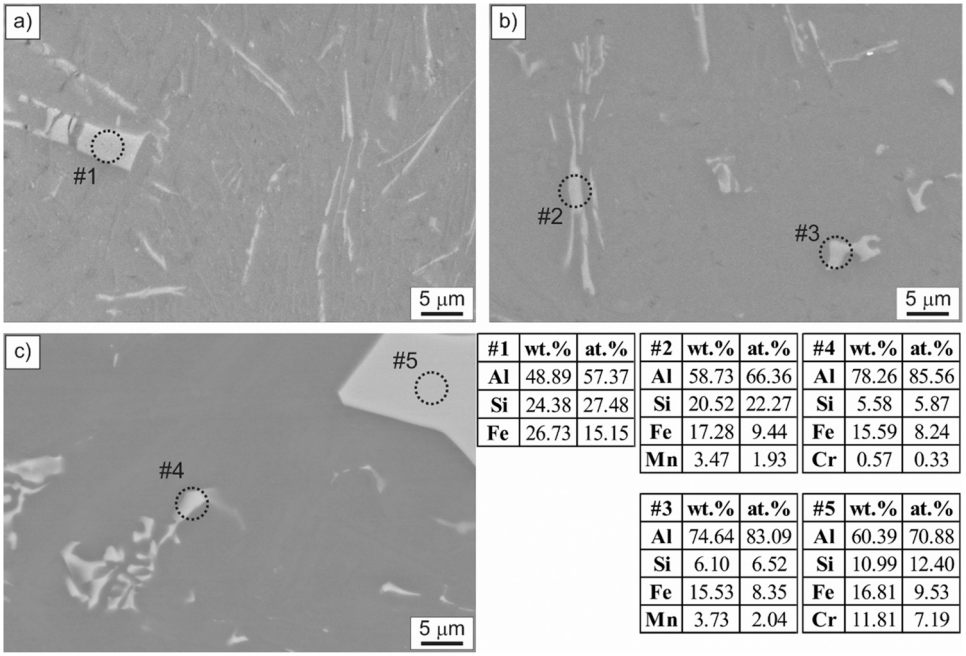

#1	wt.%	at.%
Al	48.89	57.37
Si	24.38	27.48
Fe	26.73	15.15

#2	wt.%	at.%
Al	58.73	66.36
Si	20.52	22.27
Fe	17.28	9.44
Mn	3.47	1.93

#4	wt.%	at.%
Al	78.26	85.56
Si	5.58	5.87
Fe	15.59	8.24
Cr	0.57	0.33

#3	wt.%	at.%
Al	74.64	83.09
Si	6.10	6.52
Fe	15.53	8.35
Mn	3.73	2.04

#5	wt.%	at.%
Al	60.39	70.88
Si	10.99	12.40
Fe	16.81	9.53
Cr	11.81	7.19

Fig. 9. SEM-EDS results of: a) Al-12 %Si-1 %Fe, b) Al-12 %Si-1 %Fe-1 %Mn and c) Al-12 %Si-1 %Fe-0.6 %Cr alloys at a cooling rate of 3.5 °C/s.

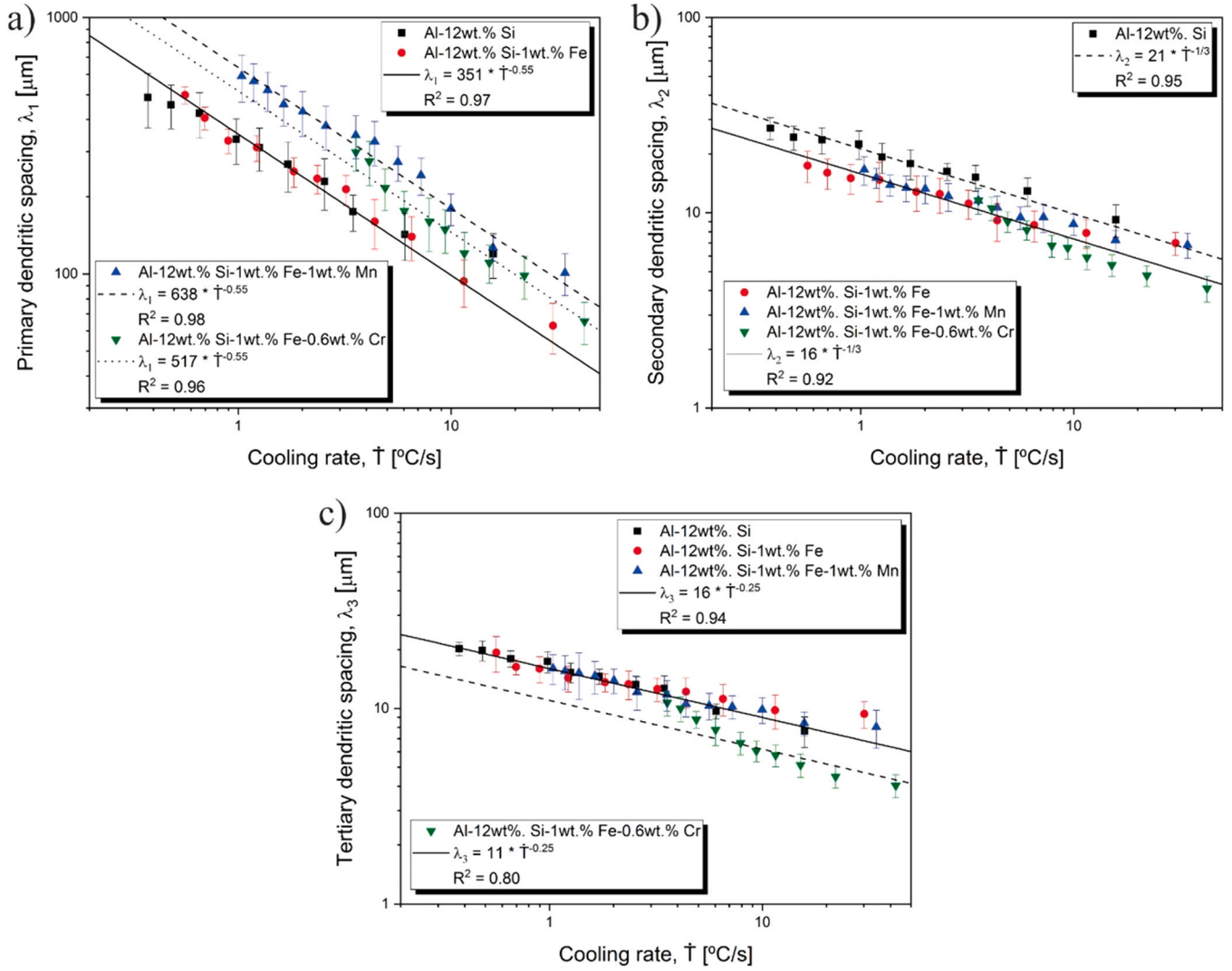

Fig. 10. Evolution of dendritic spacings as a function of cooling rate: a) primary, b) secondary and c) tertiary dendritic spacings.

3.2. Microstructural measurements and hardness

The dendritic spacings were measured and correlated with the cooling rate, following power law functions, as can be seen in Fig. 10. The exponents were based on previous works on directional solidification of Al alloys [35,36]. It is evident that the increase in cooling rate induced the refinement of the dendritic spacings whilst the influence of the alloying elements was not obvious. The inclusion of 1 %Fe in the Al-12 %Si alloy did not modify the primary dendritic spacing, but with additions of 1 %Mn and 0.6 %Cr, λ_1 became 82 % and 47 % coarser, respectively. In contrast, the alloying elements refined the secondary dendritic spacing, which decreased 24 % as compared to those of the Al-12 %Si alloy. Regarding the tertiary dendritic spacing, the refinement only occurred for the Al-12 %Si-1 %Fe-0.6 %Cr alloy (reduction of 31 %), and a single experimental correlation was able to describe the evolution of λ_3 for the other alloys examined.

The harmful effects of the β-AlFeSi phase are mainly attributed to its high brittleness, sharp edge plate morphology, and size. For plates having small size and uniform distribution in the microstructure, the ductility would not be severely affected. Hence, the size distribution of IMCs has been evaluated and can be observed in Fig. 11. The measurements were performed on three samples of each alloy casting, i.e., samples that solidified at high ($\dot{T} > 11.0$ °C/s), moderate ($\dot{T} = 6.0$ °C/s) and low ($\dot{T} = 3.5$ °C/s) cooling rates. At high cooling rates, the β-AlFeSi plates of the Al-12 %Si-1 %Fe alloy ranged from 1.1 to 723.8 μm^2, with most of them < 4 μm^2. However, due to the presence of large plates, the mean size and error (5.2 ± 2.9 μm^2) were relatively large. Decreasing to moderate $\dot{T}$, the large plates disappeared and, hence, the mean and maximum sizes significantly decreased to 3.3 and 110.0 μm^2, respectively. Comparing to the latter condition, the mean size increased by 27 % at low $\dot{T}$. In Section 3.1, it was observed that Mn acted to partially transform the β-AlFeSi plates into α-Al(Fe,Mn)Si particles having a Chinese script morphology, while Cr induced a complete presence of α-Al(Fe,Cr)Si, having morphologies characterized by fine fishbone and coarse trefoil/blocky. The three cooling rate intensities were not able to ensure the formation of α-Al(Fe,Mn)Si particles smaller than the β-AlFeSi plates of the Al-12 %Si-1 %Fe alloy casting. From the size distribution shown in Fig. 11b, it can be seen that there is a significant number of IMCs with 5.1–25 μm^2, which corresponds to β-AlFeSi particles in the Al-12 %Si-1 % Fe-1 %Mn alloy casting.

In Fig. 12a, the count per area of Al-12 %Si-1 %Fe and Al-12 %Si-1 %Fe-1 %Mn alloys castings shows a slight increasing trend with the decrease in cooling rate, but there are some relevant points to consider: (i) the increase in particles for the ternary alloy is explained by the lack of large plates, which provides greater amount of solute to form smaller plates; (ii) in the Al-12 %Si-1 %Fe-1 %Mn alloy, the size of one β-AlFeSi particle is equivalent to more than one α-Al(Fe, Mn)Si Chinese script particle, which is at the same time accompanied by increase in the fraction of α-Al(Fe, Mn)Si and coarsening of the IMCs with the decrease in $\dot{T}$; and (iii) since the amount of IMCs in the Al-12 %Si-1 %Fe alloy

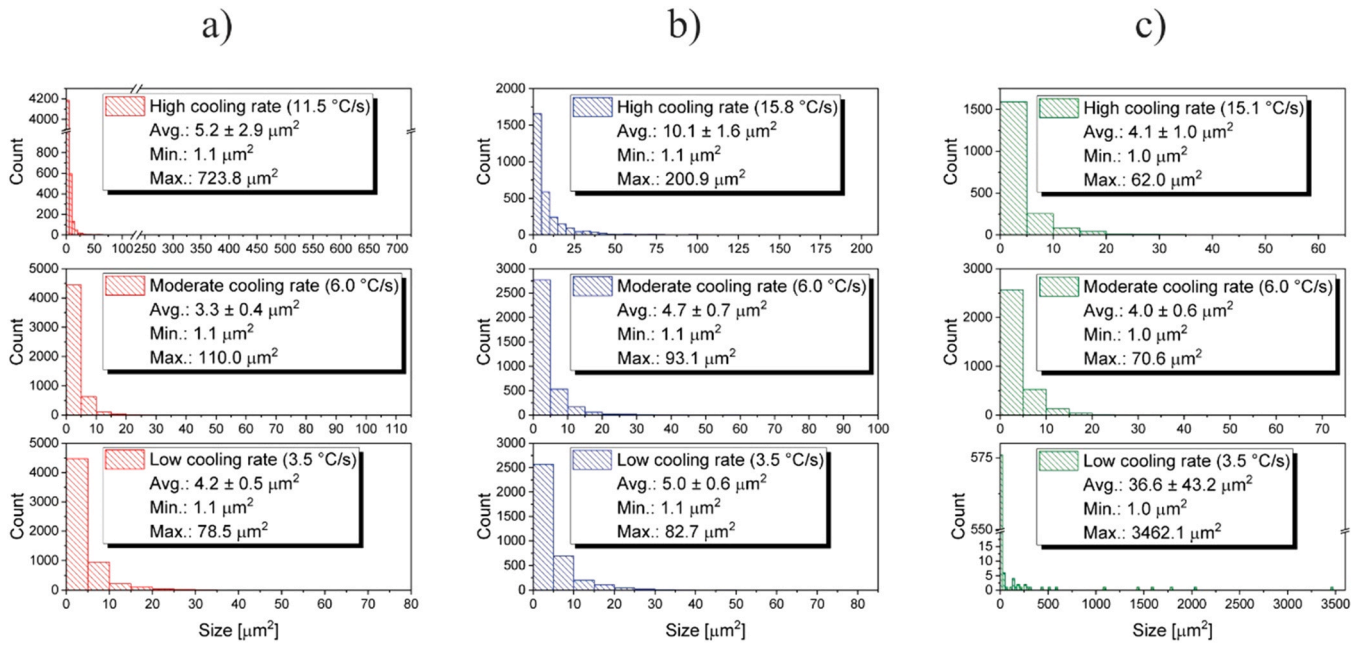

Fig. 11. The size distribution of the Fe-containing intermetallics at different cooling rates: a) Al-12 %Si-1 %Fe, b) Al-12 %Si-1 %Fe-1 %Mn and c) Al-12 %Si-1 %Fe-0.6 %Cr alloys. A single bin size (5 μm^2) was applied in the histograms.

casting is always higher (up to 35 %), it is consistent to say that the IMCs in the Al-12 %Si1 %Fe-1 %Mn alloy casting are larger.

The area fraction of Fe-contained IMCs (Fig. 12b) corroborates the microstructure observations. In the Al-12 %Si-1 %Fe alloy casting, due to the large plates, the area fraction is 4.3 % (high $\dot{T}$), decreasing to 3.3 % with the absence of large plates (moderate $\dot{T}$), and reaching 4.6 % because of the coarsening of the IMCs (low $\dot{T}$). The gradual replacement of β-AlFeSi for α-Al(Fe,Mn)Si decreased the area fraction from 5.6 % to 3.2 %, and maintained in 3.5 % at low $\dot{T}$.

The full presence of α-Al(Fe,Cr)Si particles in the Al-12 %Si-1 %Fe-0.6 %Cr alloy casting resulted in the smallest and largest IMC mean sizes (Fig. 11c). The compact fishbone is the most refined IMC, on the other hand, at low $\dot{T}$, the number of trefoil/blocky is expressive, increasing the mean size. In the transverse section, the α-Al(Fe,Cr)Si is discontinuous, leading to a high number of small particles, as can be seen in Fig. 12a, where the count per area in the Al-12 %Si1 %Fe-0.6 %Cr alloy casting is higher than 1100 units/mm^2, at high and moderate $\dot{T}$. At low $\dot{T}$, the coarse trefoil/blocky dramatically reduced the fraction of fishbone particles, and consequently, the count per area dropped to 2550 units/mm^2. In contrast, for the Al-12 %Si-1 %Fe-1 % Mn alloy casting a rising bias can be associated with the area fraction, which increases from 4.7 % to 7.5 %. As the distribution of α-Al(Fe,Cr) Si trefoil/blocky was quite irregular, the area fraction at low $\dot{T}$ presented a high standard deviation.

Through the shape factors, such as circularity and aspect ratio (Fig. 12c–d), it is clear the modification in the Fe-contained IMCs. The circularity in the Al-12 %Si-1 %Fe alloy was around 0.35, achieving 0.39 with the addition of 1 %Mn (as a result of the partial formation of α-Al (Fe,Mn)Si) and rising to 0.48 in the Al-12 %Si-1 %Fe-0.6 %Cr alloy. The lack of plates and the roundness of fishbones supported the increase in circularity. While the aspect ratio (AR) in the Al-12 %Si-1 % Fe alloy casting increased with the reduction in cooling rate, an opposite behavior was noted in the Al-12 %Si-1 %Fe-1 %Mn alloy casting. In fact, during coarsening of β-AlFeSi plates, the length tends to grow more than the width, resulting in elongated plates and a higher AR. As expected, in the Al-12 %Si-1 %Fe-1 %Mn alloy casting, the AR decreased as the fraction of α-Al(Cr,Mn)Si Chinese script increased. Even with the precipitation of trefoil/blocky, the AR in the Al-12 %Si-1 %Fe-0.6 %Cr alloy kept around 2.5.

The microhardness of the alloys was correlated with λ_3 (lowest dendritic arm spacing), following Hall-Petch type equations, as can be seen in Fig. 13a. The mechanical behavior of the alloy is a function not only of the reinforcement response of the phases formed, but also of the solid solution and the degree of refining of the microstructure. However, the correlation between hardness and λ_3 is associated with the more representative influence of the highest order dendritic spacing on the mechanical properties [37]. The experimental equations showed improvement in hardness as the dendritic spacing became more refined, however, in the specific range in which ($\lambda_3^{-1/2}$ = 0.25–0.30 $\mu m^{-1/2}$), HV of the Al-12 %Si-1 %Fe-1 %Mn alloy casting was not sensitive to λ_3. The solid solution of Si in the α-Al matrix was the same for all alloys examined, so the distinction between the equations can be attributed to the different Fe-contained IMCs. Without alloying elements to form IMCs, the Al-12 %Si alloy has only Si as a hard phase and exhibited the lowest hardness profile. In the same λ_3 range, the hardness of Al-12 % Si-1 %Fe alloy was superior to the others, thanks to the brittle β-AlFeSi IMC. The mixture of β-AlFeSi and α-Al(Fe,Mn)Si particles in the Al-12 %Si-1 %Fe-1 %Mn alloy provided a higher profile than that of the Al-12 %Si-1 %Fe-0.6 %Cr alloy, although the latter reached the highest hardness among all the alloys examined. The recognized sludge in the microstructure has been highlighted by a pink circle around the corresponding points in Fig. 13a. Although the hardness test has been randomly performed on the surface of the sample, the length of error bars around the average value of hardness is higher for points with presence of sludge. This greater variation in the values may be due to the contrast in hardness of the sludge particles (harder) with respect to the remaining phases. The indentations may be located either entirely, or partially and offlay the sludge. With a view to a better comprehension on the role of IMCs, HV was also correlated with the cooling rate (Fig. 13b), by applying a power law function. Based on the cooling rates intensities, at high $\dot{T}$, the Al-12 %Si-1 %Fe and Al-12 %Si-1 %Fe-1 %Mn alloys have equivalent hardness, whereas a value 5 % higher is related to the Al-12 %Si-1 %Fe-0.6 %Cr alloy. Probably, the minor fraction of α-Al(Fe,Mn)Si balanced the fact that the addition of Mn reduced the number of particles. Besides, the uniform distribution and size of the α-Al(Fe,Cr)Si fishbone improved the mechanical behavior. For moderate $\dot{T}$, the hardness of Al-12 %Si-1 %Fe-1 %Mn alloy is shown to be lower than the other Fe-contained alloys, matching with the increase in the α-

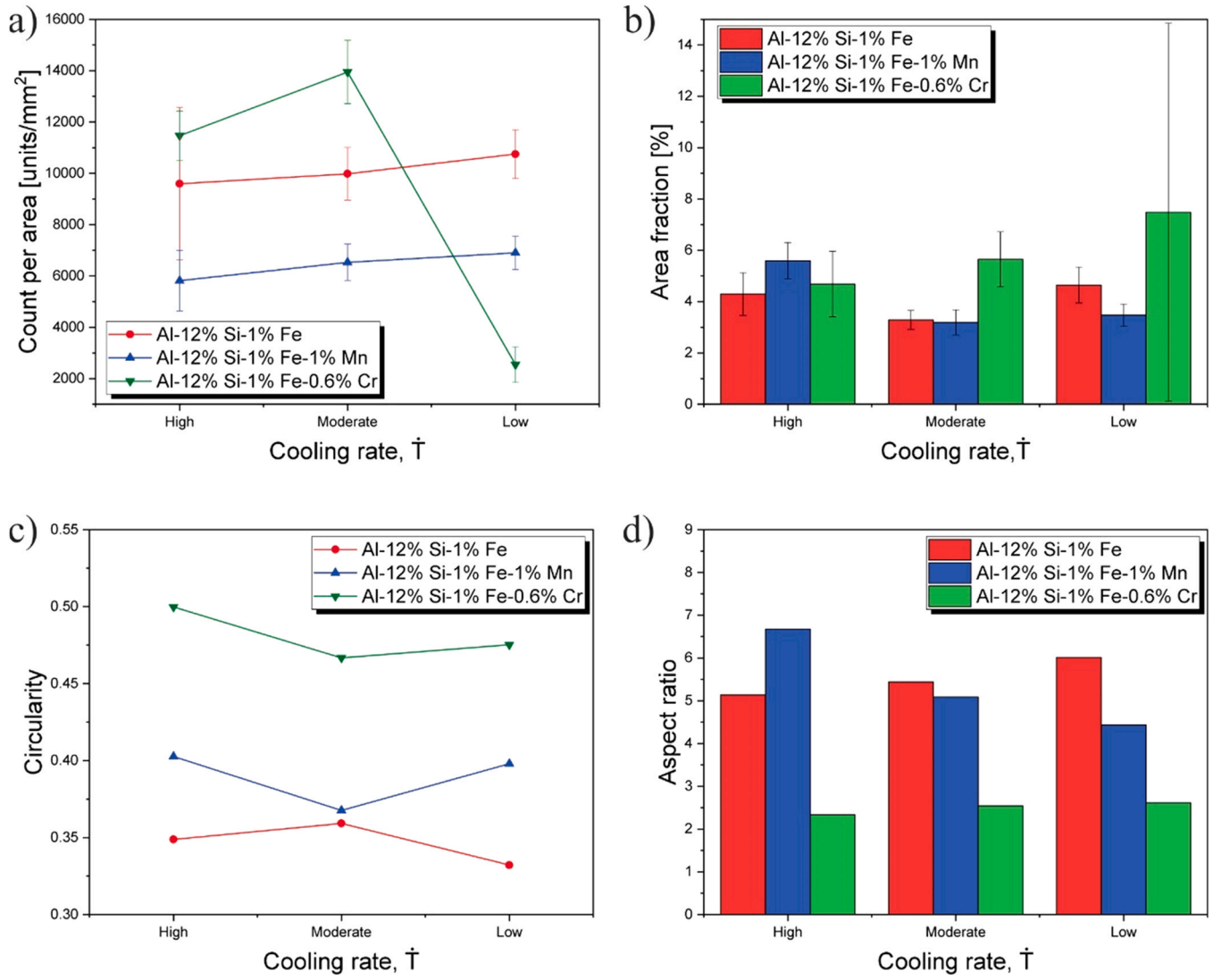

Fig. 12. The distribution of the Fe-containing IMCs in terms of a) count per area and b) area fraction at different cooling rates. The shape factors of these IMCs: c) circularity and d) aspect ratio.

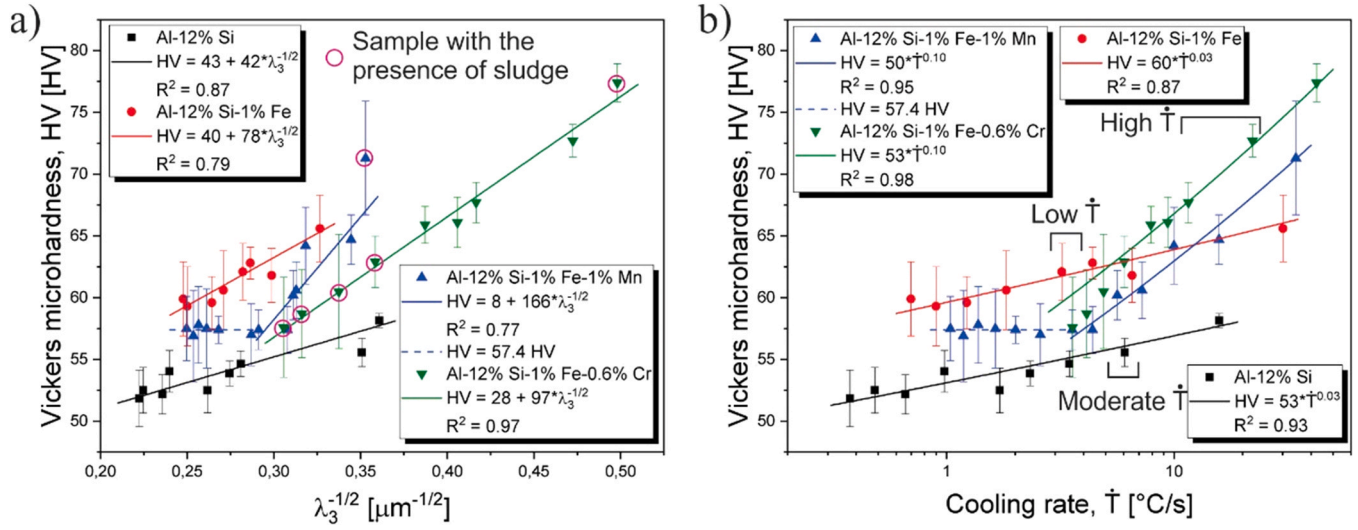

Fig. 13. Vickers microhardness of the alloys as a function of a) $(\lambda_3)^{-1/2}$ and b) cooling rate.

Al(Fe,Mn)Si Chinese script fraction. In the case of Al-12 %Si-1 %Fe-0.6 %Cr alloy, at low cooling rates, with the presence of coarse trefoil/blocky IMCs, the hardness was inferior to that of the Al-12 %Si-1 %Fe alloy. Therefore, the β-AlFeSi plates are responsible for raising the brittleness of the alloys, whereas the α-Al(Fe,Mn)Si Chinese script and the α-Al(Fe,Cr)Si fishbone particles increase hardness because of their compact morphology and better distribution in the microstructure.

4. Conclusions

- The present unsteady-state directional solidification experiments, allowed to obtain solidification cooling rates ($\dot{T}$) in the range from 0.4 to 42.3 °C/s along the length of the alloys castings experimentally examined, with a common range between 1.2 and 15.8 °C/s. For all directionally solidified (DS) alloys castings the macrostructure is characterized by columnar grains, which prevailed from bottom to top.
- The typical microstructure of the four alloys examined is characterized by an α-Al dendritic matrix with interdendritic regions formed by α-Al, Si and IMCs: Al-12 %Si alloy: the presence of Fe in both Al and Si promoted the formation of the β-AlFeSi IMC; Al-12 %Si-1 %Fe alloy: plate-like morphology IMCs; Al-12 %Si-1 %Fe-1 %Mn alloy: plate-like and Chinese script IMCs; Al-12 %Si-1 %Fe-0.6 %Cr alloy: absence of plates and predominance of compact IMCs having a fishbone morphology as well as a trefoil/blocky IMC, which depends on the local cooling rate.
- Experimental power law equations have been determined relating the primary (λ_1), secondary (λ_2) and tertiary dendritic arm spacings (λ_3) to $\dot{T}$, for any DS alloy casting experimentally examined. The addition of 1 %Fe to the Al-12 %Si alloy was shown not to affect λ_1, but with additions of 1 %Mn and 0.6 %Cr, λ_1 became 82 % and 47 % coarser, respectively. The alloying elements refined λ_2, which decreased 24 % as compared to those of the Al-12 %Si alloy. Regarding λ_3, the refinement only occurred for the Al-12 %Si-1 %Fe-0.6 %Cr alloy (31 % reduction), and a single experimental correlation was able to describe the evolution of λ_3 for the other alloys examined.
- The microhardness (HV) was correlated with λ_3 (lowest dendritic arm spacing), and Hall-Petch type equations have been determined relating HV to λ_3 for any DS alloy casting experimentally examined. The experimental equations showed improvement in HV as λ_3 became more refined, however, in the specific range in which ($\lambda_3^{-1/2} = 0.25–0.30\ \mu m^{-1/2}$), HV of the Al-12 %Si-1 %Fe-1 %Mn alloy casting was not affected by λ_3. The Al-12 %Si-1 %Fe-0.6 %Cr alloy, reached the highest HV among all the alloys examined. For a better understanding of the role of IMCs, HV was also correlated with $\dot{T}$.

Data Availability Statement

Data presented in this study are available on request from the corresponding author. Data are not publicly available because pertain to research still in development.

Declaration of Competing Interest

The authors declare that they have no known competing financial interests or personal relationships that could have appeared to influence the work reported in this paper.

Acknowledgements

The authors are grateful to São Paulo Research Foundation – FAPESP (Grant 2021/11439-0), to National Council for Scientific and Technological Development – CNPq and to FAEPEX - Fund to Support Teaching, Research and Extension (Grants: #2162/21 and #2549/22) for their financial support. This study was financed in part by the Coordenação de Aperfeiçoamento de Pessoal de Nível Superior – Brasil (CAPES) – Finance code 001.

References

[1] M.A. de Godoy Leme, R. Kakitani, C.M. Takeda, K.G. Silva, N. Cheung, M.G. Miguel, Characterization of mined metals from a Brazilian sanitary landfill, J. Sustain. Metall. 8 (2022) 1904–1914, https://doi.org/10.1007/s40831-022-00619-4
[2] J. Cui, H.J. Roven, Recycling of automotive aluminum, Trans. Nonferrous Met. Soc. China 20 (2010) 2057–2063, https://doi.org/10.1016/S1003-6326(09)60417-9
[3] S.K. Das, J.A.S. Green, J.G. Kaufman, The development of recycle-friendly automotive aluminum alloys, JOM 59 (2007) 47–51, https://doi.org/10.1007/s11837-007-0140-2
[4] H. Antrekowitsch, G. Hanko, P. Paschen, Recycling of aluminium and magnesium parts from used cars: legislative frame and consequences for metallurgy and material design, SAE Tech. Pap. (2001) 2001–01–3778, https://doi.org/10.4271/2001-01-3778
[5] A.K. Prasada Rao, W.Q. Ain, M.K. Faisal, B.I. Mazni, Undiluted recycling of aluminum scrap alloy using Hume-Rothery's rule, Metallogr. Microstruct. Anal. 7 (2018) 239–244, https://doi.org/10.1007/s13632-018-0431-8
[6] G. Gaustad, E. Olivetti, R. Kirchain, Improving aluminum recycling: a survey of sorting and impurity removal technologies, Resour. Conserv. Recycl. 58 (2012) 79–87, https://doi.org/10.1016/j.resconrec.2011.10.010
[7] P.N. Crepeau, Effect of iron in Al-Si casting alloys: a critical review, Trans. AFS 103 (1995) 361–366.
[8] C.B. Basak, N. Hari Babu, Improved recyclability of cast Al-alloys by engineering β-$Al_9Fe_2Si_2$ phase, in: A. Ratvik (Ed.), Light Met, 2017 2017, pp. 1139–1147, https://doi.org/10.1007/978-3-319-51541-0_137
[9] N.A. Belov, A.A. Aksenov, D.G. Eskin, Iron in Aluminium Alloys: Impurity and Alloying Element, first ed., Taylor & Francis Inc., New York, 2002.
[10] M. Mahta, M. Emamy, A. Daman, A. Keyvani, J. Campbell, Precipitation of Fe rich intermetallics in Cr- and Co-modified A413 alloy, Int. J. Cast Met. Res. 18 (2005) 73–79, https://doi.org/10.1179/136404605225022928
[11] X. Song, M. Gao, B. Yang, R. Guan, Modification and refinement of Fe-containing phases, mechanical properties and strengthening mechanisms in Al–Fe alloys via Cr alloying and continuous rheo-extrusion, Mater. Sci. Eng. A 850 (2022) 143557, https://doi.org/10.1016/j.msea.2022.143557
[12] S. Ferraro, G. Timelli, Influence of sludge particles on the tensile properties of die-cast secondary aluminum alloys, Metall. Mater. Trans. B 46 (2015) 1022–1034, https://doi.org/10.1007/s11663-014-0260-3
[13] X. Zhang, D. Wang, X. Li, H. Zhang, H. Nagaumi, Understanding crystal structure and morphology evolution of Fe, Mn, Cr-containing phases in Al-Si cast alloy, Intermetallics 131 (2021) 107103, https://doi.org/10.1016/j.intermet.2021.107103
[14] B.H. Kim, S.M. Lee, H. Yasuda, Morphological variation of Fe/Cr-rich intermetallic phase in recycled Al-Si alloy as a function of solidification rate: time-resolved radiography, Mater. Sci. Forum 654–656 (2010) 974–977, https://doi.org/10.4028/www.scientific.net/MSF.654-656.974
[15] W. Eidhed, Modification of β-Al_5FeSi compound in recycled Al-Si-Fe cast alloy by using Sr, Mg and Cr additions, J. Mater. Sci. Technol. 24 (2008) 45–48.
[16] C. Silva, A. Barros, A.V. Rodrigues, R. Kakitani, T. Soares, A. Garcia, N. Cheung, Microstructure and tensile strength of an Al-Si-Fe-V alloy: vanadium and solidification thermal parameters as recycling strategies, Sustainability 14 (2022) 13859, https://doi.org/10.3390/su142113859
[17] S.G. Shabestari, The effect of iron and manganese on the formation of intermetallic compounds in aluminum–silicon alloys, Mater. Sci. Eng. A 383 (2004) 289–298, https://doi.org/10.1016/j.msea.2004.06.022
[18] B. Wang, J. Wang, X. Liu, Q. Li, X. Liu, Uncovering the effects of neutralizing elements (Co, Mn and Cr) on the Fe-rich intermetallic formation in Al–Si–Cu alloys, Mater. Sci. Eng. A 858 (2022) 144090, https://doi.org/10.1016/j.msea.2022.144090
[19] G. Timelli, A. Fabrizi, S. Capuzzi, F. Bonollo, S. Ferraro, The role of Cr additions and Fe-rich compounds on microstructural features and impact toughness of AlSi9Cu3(Fe) diecasting alloys, Mater. Sci. Eng. A 603 (2014) 58–68, https://doi.org/10.1016/j.msea.2014.02.071
[20] J.M. Sanchez, M. Arribas, H. Galarraga, M. Garcia de Cortazar, M. Ellero, F. Girot, Effects of Mn addittion, cooling rate and holding temperature on the modification and purification of iron-rich compounds in AlSi10MnMg(Fe) alloy, Heliyon 9 (2023) e13005, https://doi.org/10.1016/j.heliyon.2023.e13005
[21] K. Liu, X. Cao, X.-G. Chen, Effect of Mn, Si, and cooling rate on the formation of iron-rich intermetallics in 206 Al-Cu cast alloys, Metall. Mater. Trans. B 43 (2012) 1231–1240, https://doi.org/10.1007/s11663-012-9694-7
[22] S. Seifeddine, S. Johansson, I.L. Svensson, The influence of cooling rate and manganese content on the β-Al5FeSi phase formation and mechanical properties of Al–Si-based alloys, Mater. Sci. Eng. A 490 (2008) 385–390, https://doi.org/10.1016/j.msea.2008.01.056
[23] D. Song, Y. Zhao, Y. Jia, R. Li, N. Zhou, K. Zheng, Y. Fu, W. Zhang, Study of the evolution mechanisms of Fe-rich phases in Al-Si-Fe alloys with Mn modification using synchrotron X-ray imaging, J. Alloy. Compd. 915 (2022) 165378, https://doi.org/10.1016/j.jallcom.2022.165378
[24] M. Gündüz, E. Çadırlı, Directional solidification of aluminium–copper alloys, Mater. Sci. Eng. A 327 (2002) 167–185, https://doi.org/10.1016/S0921-5093(01)01649-5
[25] R. Kakitani, A. Garcia, N. Cheung, Morphology of intermetallics tailoring tensile properties and quality index of a eutectic Al–Si–Ni alloy, Adv. Eng. Mater. 22 (2020) 2000503, https://doi.org/10.1002/adem.202000503

[26] L. Zuo, B. Ye, J. Feng, X. Xu, X. Kong, H. Jiang, Effect of δ-Al3CuNi phase and thermal exposure on microstructure and mechanical properties of Al-Si-Cu-Ni alloys, J. Alloy. Compd. 791 (2019) 1015–1024, https://doi.org/10.1016/j.jallcom.2019.03.412
[27] Y. Yang, S.-Y. Zhong, Z. Chen, M. Wang, N. Ma, H. Wang, Effect of Cr content and heat-treatment on the high temperature strength of eutectic Al–Si alloys, J. Alloy. Compd. 647 (2015) 63–69, https://doi.org/10.1016/j.jallcom.2015.05.167
[28] Y. Zhang, H. Zheng, Y. Liu, L. Shi, R. Xu, X. Tian, Cluster-assisted nucleation of silicon phase in hypoeutectic Al–Si alloy with further inoculation, Acta Mater. 70 (2014) 162–173, https://doi.org/10.1016/j.actamat.2014.01.061
[29] X. Lan, K. Li, J. Wang, M. Yang, Q. Lu, Y. Du, Developing Al–Fe–Si alloys with high thermal stability through tuning Fe, Si contents and cooling rates, Intermetallics 144 (2022) 107505, https://doi.org/10.1016/j.intermet.2022.107505
[30] E. Cinkilic, C.D. Ridgeway, X. Yan, A.A. Luo, A formation map of iron-containing intermetallic phases in recycled cast aluminum alloys, Metall. Mater. Trans. A 50 (2019) 5945–5956, https://doi.org/10.1007/s11661-019-05469-6
[31] L. Zhang, J. Gao, L.N.W. Damoah, D.G. Robertson, Removal of iron from aluminum: a review, Miner. Process. Extr. Metall. Rev. 33 (2012) 99–157, https://doi.org/10.1080/08827508.2010.542211
[32] G. Timelli, S. Capuzzi, A. Fabrizi, Precipitation of primary Fe-rich compounds in secondary AlSi9Cu3(Fe) alloys, J. Therm. Anal. Calorim. 123 (2016) 249–262, https://doi.org/10.1007/s10973-015-4952-y
[33] S. Ferraro, A. Bjurenstedt, S. Seifeddine, On the formation of sludge intermetallic particles in secondary aluminum alloys, Metall. Mater. Trans. A Phys. Metall. Mater. Sci. 46 (2015) 3713–3722, https://doi.org/10.1007/s11661-015-2942-0
[34] T. Liu, M. Karkkainen, L. Nastac, V. Arvikar, I. Levin, L.N. Brewer, Iron-rich intermetallics in high pressure die cast A383 aluminum alloys, Intermetallics 126 (2020) 106814, https://doi.org/10.1016/j.intermet.2020.106814
[35] R. Kakitani, C.B. Cruz, T.S. Lima, C. Brito, A. Garcia, N. Cheung, Transient directional solidification of a eutectic Al–Si–Ni alloy: macrostructure, microstructure, dendritic growth and hardness, Materialia 7 (2019) 100358, https://doi.org/10.1016/j.mtla.2019.100358
[36] M.V. Canté, T.S. Lima, C. Brito, A. Garcia, N. Cheung, J.E. Spinelli, An alternative to the recycling of Fe-contaminated Al, J. Sustain. Metall. 4 (2018) 412–426, https://doi.org/10.1007/s40831-018-0188-y
[37] J. Campbell, Complete Casting Handbook: Metal Casting Processes, Metallurgy, Techniques and Design, second ed., Butterworth-Heinemann, Oxford, 2015.